Supplementary Information

Bisphosphonium cation based metal halide glass scintillators with tunable melting points

Jian-Bin Luo,§ Jun-Hua Wei,§ Zi-Lin He, Jing-Hua Chen, Qing-Peng Peng, Zhi-Zhong Zhang, and Dai-Bin Kuang*

Key Laboratory of Bioinorganic and Synthetic Chemistry of Ministry of Education,

LIFM, GBRCE for Functional Molecular Engineering, School of Chemistry, IGCME,

Sun Yat-Sen University, Guangzhou 510275, China.

*Corresponding author. Email: kuangdb@mail.sysu.edu.cn.

§Equally contributed to this work.

Experimental Section

Materials.1,4-Bis(diphenylphosphino)butane (Bidepharm, 97%), 1,5-bis(diphenylphosphino)pentane (Bidepharm, 97%), 1,6-bis(diphenylphosphino)hexane (Bidepharm, 97%), Toluene (Guangzhou Chemical Reagent, A.R.), benzyl bromide (Aladdin, >98%), 3,4-difluorobenzyl bromide (Bidepharm, >99%), 2,3-difluorobenzyl bromide(Bidepharm, >99%), 2,6-difluorobenzyl bromide(Bidepharm, >99%), manganese (II) bromide tetrahydrate ($MnBr_2 \cdot 4H_2O$, Aladdin, 98%), anhydrous methanol (MeOH, Guangzhou Chemical Reagent, A.R.), ethyl acetate (General reagent, A.R.), ether (Guangzhou Chemical Reagent, A.R.). The standard scintillators of Ce^{3+}-doped $Lu_3Al_5O_{12}$ (LuAG: Ce) crystal and bismuth germanate (BGO) were purchased from EPIC Crystal Inc. All materials were used without any purification.

Preparation of BisPP-Br powder. The bisphosphine compounds and benzyl bromide (or its derivatives) with a molar ratio of 1:1 were dissolved in toluene. The mixture was stirred at 115 °C for 3 hours, resulting in a white powder. The mixture was then naturally cooled to room temperature. Subsequently, the white powders were collected via vacuum filtration and washed for multiple times with ethyl acetate. The washed white powder is thoroughly dried in an oven.

Preparation of (BisPP)$MnBr_4$ single crystal. Generally, all crystals were synthesized using a solvothermal method by using methanol as the solvent. A mixture of BisPP-Br and $MnBr_2 \cdot 4H_2O$ with different ratios was added to methanol to form the crystal growth precursor. The reaction mixture was loaded into a Teflon autoclave and then sealed in a stainless steel Parr autoclave. The mixture was heated at 100 °C for 6 hours and then cooled to 25 °C within 12 hours. Finally, the green crystals collected by filtration were washed with ether and dried at 70 °C.

(But-bz)$MnBr_4$, (Pent-bz)$MnBr_4$, and (Hex-bz)$MnBr_4 \cdot$MeOH : The BisPP-Br and $MnBr_2 \cdot 4H_2O$ with a molar ratio of 1:2 were dissolved in methanol to form the reaction precursor.

(Hex-bz)$MnBr_4$: The BisPP-Br and $MnBr_2 \cdot 4H_2O$ with a molar ratio of 1:2 were dissolved in methanol/water (2:1) mixed solvent to form the reaction precursor.

(Hex-3,4-2F)$MnBr_4 \cdot$MeOH, (Hex-2,3-2F)$MnBr_4 \cdot$MeOH, and (Hex-2,6-2F)$MnBr_4 \cdot$MeOH: The BisPP-Br and $MnBr_2 \cdot 4H_2O$ with a molar ratio of 1:1 were dissolved in methanol to form the reaction precursor.

(But-3,4-2F)$MnBr_4$: The BisPP-Br and $MnBr_2 \cdot 4H_2O$ with a molar ratio of 1:2 were dissolved in methanol to form the reaction precursor.

Preparation of $(BisPP)_2MnBr_4$ glass. All OIMH glasses were prepared using the melt-quenched method. Generally, the $(BisPP)_2MnBr_4$ crystals were placed in a silicone mold and heated in a muffle furnace for 10-15 minutes to form a homogenous melt. Subsequently, the melt was transferred to another vacuum-drying oven preheated to the same temperature, which

was evacuated and heated for 10-15 minutes to remove the visible bubbles. The debubbling melts were then naturally cooled to room temperature. Finally, transparent glass was obtained by demolding. The heating temperatures for different OIMH are as follows: (But-bz)$MnBr_4$: 300 ℃; (Pent-bz)$MnBr_4$: 300 ℃; (Hex-bz)$MnBr_4$: 270 ℃; (Hex-3,4-2F)$MnBr_4$·MeOH: 220 ℃; (Hex-2,3-2F)$MnBr_4$·MeOH:240 ℃; and (Hex-2,6-2F)$MnBr_4$·MeOH: 240 ℃. Within the range below the decomposition temperature, the heating temperature can be appropriately increased to enhance processing performance.

Crystallography. Single-crystal X-ray diffraction measurement (SCXRD) was carried out on Rigaku XtaLAB Synergy diffractometer with Mo Kα radiation (λ = 0.71073 Å) and Cu Kα radiation (λ = 1.54184Å). The structures were solved by the intrinsic phasing method (SHELXT) and refined by the SHELXL refinement package using the Least Squares minimization method. VESTA software was used to visualize the crystal structure. [1] Room temperature powder X-ray diffraction (PXRD) measurement was performed on a Miniflex 600 diffractometer (Rigaku) and SmartLab diffractometer (Rigaku) with Cu Kα radiation (λ = 1.54 Å). Temperature-dependent PXRD data were collected on SmartLab diffractometer (Rigaku). The crystallographic data can be obtained from the Cambridge Crystallographic Data Centre (CCDC) with the accession number of 2349445 - 2349452.

Thermodynamics analysis. Thermogravimetric analysis (TGA) was conducted by using the Netzsch TG 209F1 Libra instrument. The sample was heated from room temperature to 800 °C at the rate of 10 °C/min under nitrogen flow. Additionally, the TG-IR test was conducted using the STA449F3/Nicolet 6700 apparatus with a heating rate of 10 °C/min under nitrogen atmosphere. The differential scanning calorimetry (DSC) analysis was performed on the Netzsch DSC 214 instrument. The sample was heated at a rate of 10 °C/min in a nitrogen atmosphere. After reaching the target temperature, the sample was cooled down to room temperature at a rate of 10 °C/min, and then a second heat-up scan was initiated to determine the glass transition temperature. The T_m and T_g were determined by the NETZSCH Proteus software.

Optical properties. Room temperature steady-state and time-resolved photoluminescence spectra were acquired on the FLS980 instrument (Edinburgh Instruments LTD). Photoluminescence quantum yields (PLQYs) were recorded on the Hamamatsu C9920 system. The transmittance spectrum of the OIMH glass sample was recorded using a Shimadzu UV 3600 spectrophotometer equipped with an integrated sphere, and $BaSO_4$ was used as the reference. The FTIR spectra were recorded on a PerkinElmer Frontier spectrophotometer equipped with an attenuated total reflection (ATR) module. Raman measurements were conducted through a Renishaw InVia Reflex confocal Raman spectrometer equipped with an NIR laser (λ = 785 nm) acting as the excitation source.

X-ray attenuation efficiency. The calculation of attenuation efficiency (%) allows for the assessment of materials' attenuation capability towards X-rays. The X-tay attenuation efficiency can be calculated using the following equation: [2]

$$\mathrm{AE} = \left(1 - e^{-t\rho d}\right) \times 100\%$$

Here, *t* represents the total attenuation coefficient obtained from the XCOM database of the National Institute of Standards and Technology (NIST). ρ denotes the density(g/cm^3) and *d* denotes the thickness(cm).

X-ray scintillation properties. The determination of the sample's light yield follows a reference method, utilizing commercial LuAG: Ce crystal as the primary reference and combining BGO as the secondary reference. To conduct the measurements, an Amptek Mini-X2 X-ray tube with a silver (Ag) target was used as the X-ray source and an Ocean Optics portable spectrometer (QEpro) equipped with an integrating sphere was used to collect the photons. The crystals were pressed into wafers, and the glass sample was obtained by in-situ melt-quenching the crystals inside the quartz vessel. The sample was carefully loaded into a quartz vessel, which was then placed inside the integrating sphere. The measured photon counts are normalized to 100 % X-ray attenuation by employing the following formula: [2]

$$\mathrm{P}_{normlized} = \frac{P_{measured}}{AE(d)}$$

where AE(d) denotes the attenuation efficiency (%) of sample at its thickness. The light yield (LY) can be calculated by the following equation: [2]

$$LY_{sample} = LY_{LuAG:Ce} \times \frac{P_{normalized}(Sample)}{P_{normalized}(LuAG:Ce)}$$

The Hamamatsu H10721-210 photomultiplier tube was utilized to collect photons generated by the sample under different X-ray dose rates and convert them into signal currents. The signal current in the absence of X-rays was determined as the dark noise. The limit of detection was determined as the dose rate when the signal-to-noise ratio (SNR) equals 3. The dose rate of the incident X-rays was adjusted by changing the X-ray tube current, and the dose rate was calibrated through the Radical X-ray dosimeter.

Computational methods. The interaction energies of ion pairs were calculated with the Gaussian 16 program. [3] The geometries of the anion−cation complex were optimized on 6-31G (d)/B3LYP level. Their anion−cation interaction energies were calculated on 6-311G (d)/B3LYP level. For the Mn element, an SDD basis set was employed. The electrostatic potentials were calculated on def2-tzvp/B3LYP level based on the optimized cations. The rest of density-functional theory (DFT) calculations were performed by using the CP2K software package. [4] PBE with Grimme D3 correction was used to describe the system. Unrestricted Kohn-Sham DFT has been used as the electronic structure method in the framework of the Gaussian and plane waves method. The Goedecker-Teter-Hutter (GTH) pseudopotentials and

DZVP-MOLOPT-GTH basis sets were utilized to describe the molecules. A plane-wave energy cut-off of 500 Ry has been employed. The excited states of the $(BisPP)_2MnBr_4$ were calculated through Δ self-consistent field (ΔSCF) method. One Mn ion in the cell is excited, experiencing a spin-flip transition process, and its state density is calculated. The density of states (DOS) and electrostatic potential analysis were carried out on Multiwfn software. [5-7]

Supplementary Tables

Table S1. Single-crystal X-ray diffraction data of (But-bz)$MnBr_4$, (Pent-bz)$MnBr_4$, (Hex-bz)$MnBr_4$ single crystals.

Compound	(But-bz)$MnBr_4$	(Pent-bz)$MnBr_4$	(Hex-bz)$MnBr_4$
Formula	$C_{42}H_{42}Br_4MnP_2$	$C_{43}H_{44}Br_4MnP_2$	$C_{44}H_{46}Br_4MnP_2$
Formula weight	983.27	997.30	1011.33
Temperature/K	100.00(10)	293(2)	101(1)
Crystal system	monoclinic	monoclinic	orthorhombic
Space group	I2/a	P21/n	Pbca
a/Å	16.1667(7)	12.01730(10)	15.4957(10)
b/Å	13.9159(5)	13.33120(10)	33.2381(11)
c/Å	18.6147(8)	27.3180(3)	16.6711(5)
α/°	90	90	90
β/°	106.908(4)	102.6600(10)	90
γ/°	90	90	90
Volume/Å^3	4006.8(3)	4270.08(7)	8586.4(7)
Z	4	4	8
ρ_{calc}g/cm^3	1.630	1.551	1.565
μ/mm^{-1}	4.427	7.818	4.134
F(000)	1956.0	1988.0	4040.0
Radiation	Mo Kα (λ = 0.71073)	Cu Kα (λ = 1.54184)	Mo Kα (λ = 0.71073)

Table S2. Optical properties of (But-bz)$MnBr_4$, (Pent-bz)$MnBr_4$, (Hex-bz)$MnBr_4$ crystal and other Bisphosphonium Cation Based metal halide.

	Emission peak	FWHM	TRPL	PLQY	Ref
(But-bz)$MnBr_4$	530 nm	50.5 nm	295.6 μs	99.9%	This work
(Pent-bz)$MnBr_4$	517 nm	46.5 nm	295.8 μs	96.0%	This work
(Hex-bz)$MnBr_4$	539 nm	73.8 nm	274.1 μs	66.7%	This work
($C_{38}H_{34}P_2$)$MnBr_4$	517 nm	51 nm	318 μs	95%	Ref.8
($C_{40}H_{38}P_2$)$MnBr_4$	518 nm	65 nm	331 μs	74.2%	Ref.9
$C_{40}H_{38}P_2MnBr_4$	511 nm	36 nm	324 μs	84.26%	Ref.10
***p*-$C_{44}H_{38}P_2MnBr_4$**	517 nm	43 nm	308 μs	85.52%	
***o*-$C_{44}H_{38}P_2MnBr_4$**	517 nm	43 nm	290 μs	95.93%	
$C_{48}H_{38}P_2MnBr_2$	529 nm	52 nm	182 μs	30.69%	

Table S3. Decay rates of (But-bz)$MnBr_4$, (Pent-bz)$MnBr_4$, (Hex-bz)$MnBr_4$ and (Hex-bz)$MnBr_4$·MeOH crystals.

	TRPL	PLQY	k_r	k_{nr}
(But-bz)$MnBr_4$	295.6 μs	99.9%	$3.380\times10^3\ s^{-1}$	$3.383\times10^0\ s^{-1}$
(Pent-bz)$MnBr_4$	295.8 μs	96.0%	$3.245\times10^3\ s^{-1}$	$1.352\times10^2\ s^{-1}$
(Hex-bz)$MnBr_4$	274.1 μs	66.7%	$2.433\times10^3\ s^{-1}$	$1.215\times10^3\ s^{-1}$
(Hex-bz)$MnBr_4$·MeOH	290.3 μs	73.4%	$2.528\times10^3\ s^{-1}$	$9.163\times10^2\ s^{-1}$

k_r is the radiative decay rate, and k_{nr} is the non-radiative decay rate.

Table S4. Single-crystal X-ray diffraction data of (Hex-3,4-2F)$MnBr_4$·MeOH , (Hex-2,3-2F)$MnBr_4$·MeOH, and (Hex-2,6-2F)$MnBr_4$·MeOH single crystals.

Compound	(Hex-3,4-2F)$MnBr_4$·MeOH	(Hex-2,3-2F)$MnBr_4$·MeOH	(Hex-2,6-2F)$MnBr_4$·MeOH
Formula	$C_{45}H_{46}Br_4F_4MnOP_2$	$C_{45}H_{46}Br_4F_4MnOP_2$	$C_{45}H_{46}Br_4F_4MnOP_2$
Formula weight	1115.34	1115.34	1115.34
Temperature/K	100.00(10)	100.02(10)	100.00(10)
Crystal system	monoclinic	monoclinic	monoclinic
Space group	Cc	Cc	Cc
a/Å	12.2655(2)	11.8477(3)	11.5253(2)
b/Å	19.6016(3)	19.6629(4)	19.8357(3)
c/Å	19.2241(3)	19.6960(4)	20.0972(3)
α/°	90	90	90
β/°	96.3610(10)	95.412(2)	93.2590(10)
γ/°	90	90	90
Volume/Å^3	4593.47(13)	4567.93(18)	4587.04(13)
Z	4	4	4
ρ_{calc}g/cm^3	1.613	1.622	1.615
μ/mm^{-1}	3.886	3.908	3.891
F(000)	2220.0	2220.0	2220.0
Radiation	Mo Kα (λ = 0.71073)	Mo Kα (λ = 0.71073)	Mo Kα (λ = 0.71073)

Table S5. The reduced temperature (T_{rg}) of OIMHs and other inorganic materials.

Compound	T_g (°C)	T_m (°C)	T_{rg}	Ref
(But-bz)$MnBr_4$	109	281	0.69	This work
(Pent-bz)$MnBr_4$	102	268	0.69	This work
(Hex-bz)$MnBr_4$	98	225	0.75	This work
(Hex-3,4-2F)$MnBr_4$·MeOH	100	180	0.82	This work
(Hex-2,3-2F)$MnBr_4$·MeOH	94	197	0.78	This work
(Hex-2,6-2F)$MnBr_4$·MeOH	102	208	0.78	This work
$(ETP)_2MnBr_4$	50	168	0.73	Ref. 11
$(MTP)_2SbBr_5$	65	178	0.75	Ref. 12
SiO_2	~1475K	1713	0.73	Ref. 13

Table S6. PLQYs of the melt-quenched glasses in this work.

Melt-quenched glass	PLQY (%)
(But-bz)$MnBr_4$	28.3
(Pent-bz)$MnBr_4$	35.9
(Hex-bz)$MnBr_4$	25.3
(Hex-3,4-2F)$MnBr_4$	47.6
(Hex-2,3-2F)$MnBr_4$	41.9
(Hex-2,6-2F)$MnBr_4$	35.8

Table S7. Comparison of X-ray imaging spatial resolution for different metal halide glasses.

Sample	Spatial resolution (lp/mm)	Ref
(Hex-3,4-2F)$MnBr_4$ glass	25	This work
$(HTPP)_2MnBr_4$ glass	10	Ref.14
$(DOTG)_2MnBr_4$ glass	12	Ref.15
HTP_2MnBr_4 glass	17.28	Ref.16
$(BTP)_2MnBr_4$ glass-ceramic	14.25	Ref.17
$[Cu_4I_4(PPh_2Et)_4]$ glass	30	Ref.18
$(MTP)_2Cu_4I_6$ glass-ceramic	20	Ref.19
$(C_{20}H_{20}P)_2SbCl_5$ glass	30	Ref.20
$(ETP)_2SbCl_5$ wafer	19	Ref.21

Supplementary Schemes

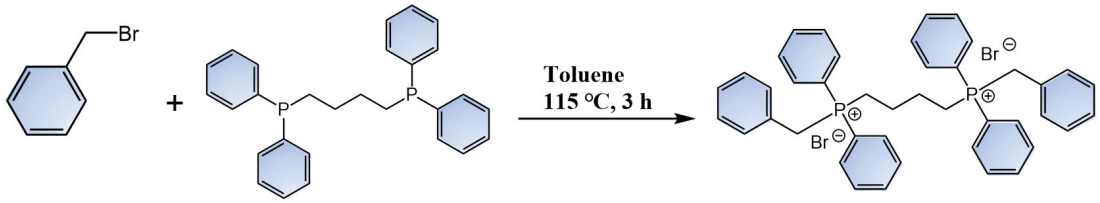

Scheme S1. The synthesis process of BisPP-Br by taking But-bz as an example.

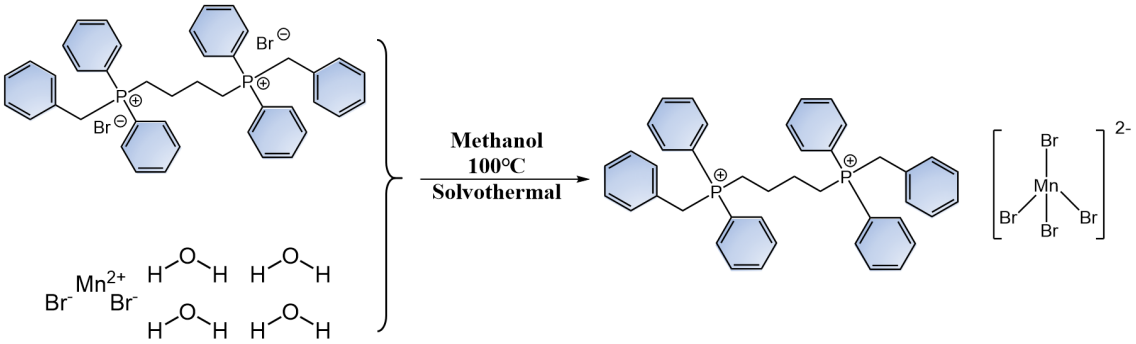

Scheme S2. The synthesis process of $(BisPP)_2MnBr_4$ single crystals by taking $(But\text{-}bz)MnBr_4$ as an example.

Supplementary Figures

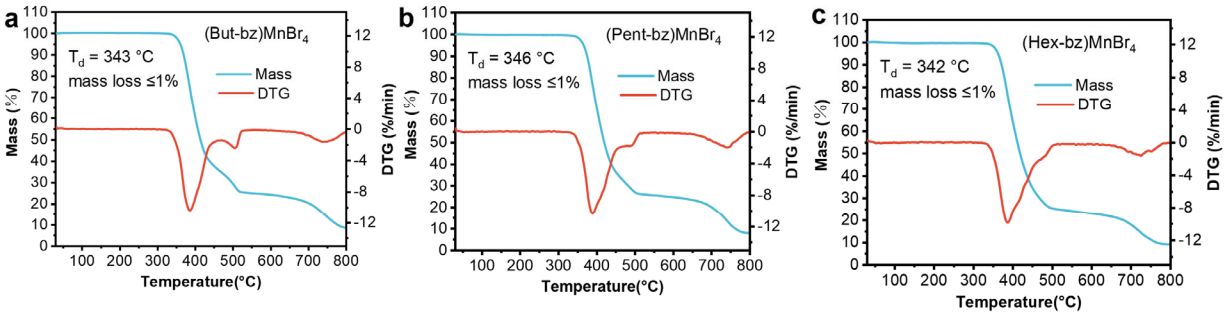

Figure S1. Thermogravimetric analysis (TGA) of crystalline a). (But-bz)$MnBr_4$, b). (Pent-bz)$MnBr_4$, and c). (Hex-bz)$MnBr_4$.

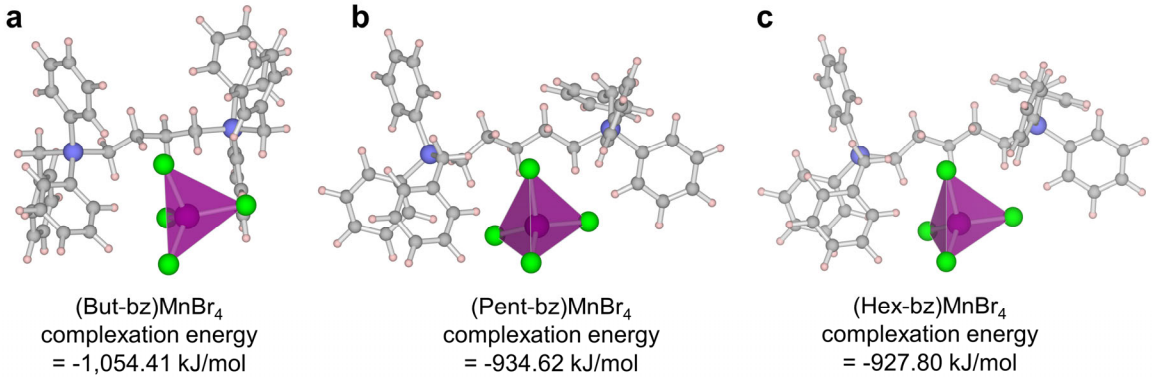

Figure S2. Complexation energies of the ion pairs. All ion pairs were optimized were optimized on 6-31G (d)/B3LYP level. Their anion−cation interaction energies were calculated on 6-311G (d)/B3LYP level.

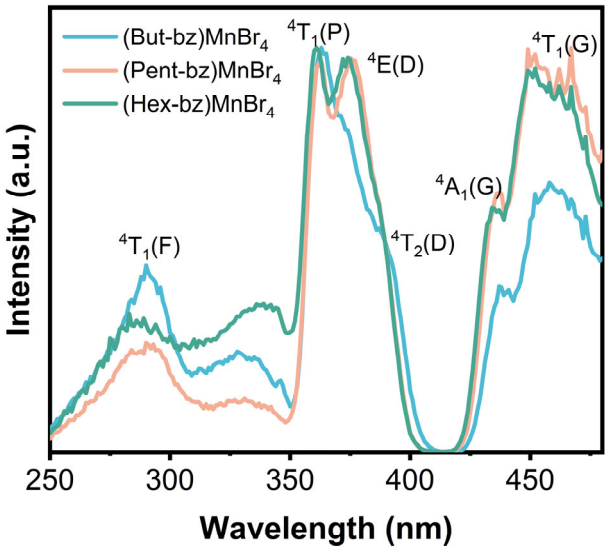

Figure S3. PLE spectra of the $(BisPP)_2MnBr_4$ crystals.

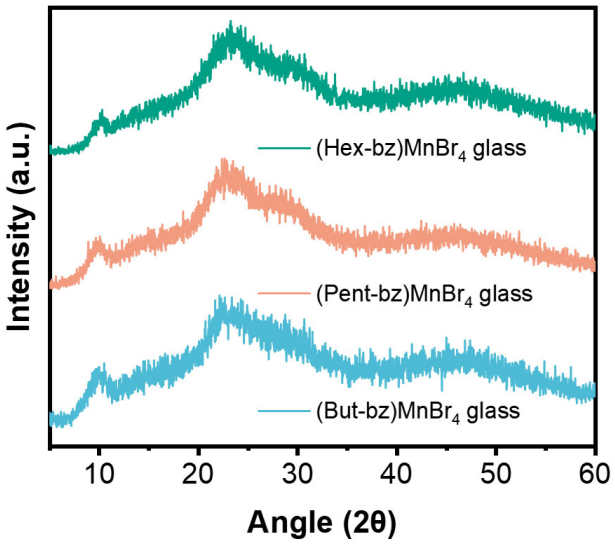

Figure S4. XRD patterns of the melt-quenched glasses of $(BisPP)MnBr_4$.

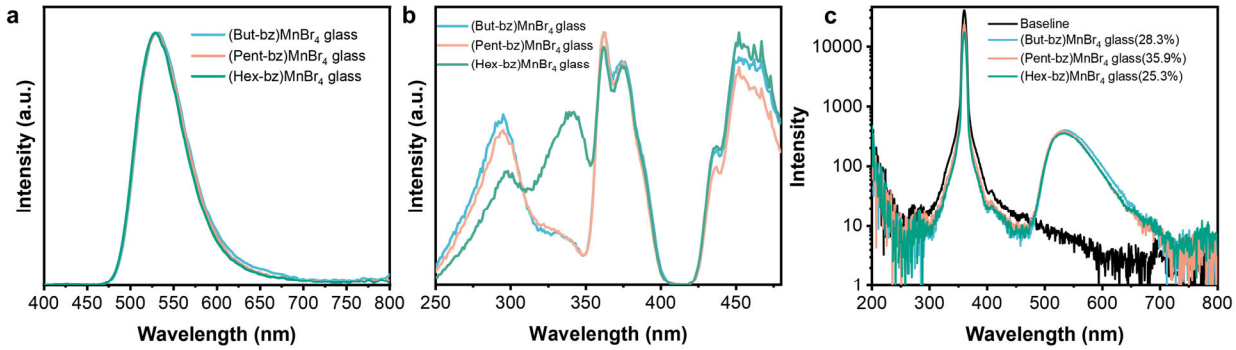

Figure S5. Optical properties of the melt-quenched OIMH glasses. a). PL spectrum, b). PLE spectrum, c). PLQY plots.

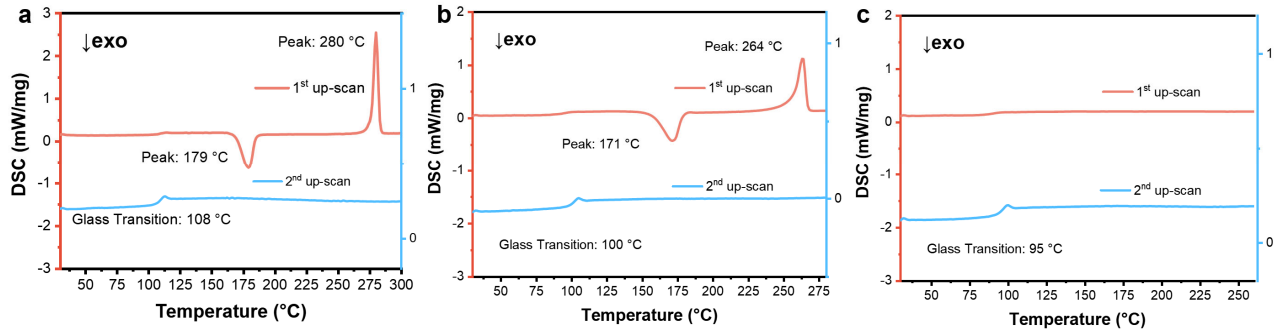

Figure S6. DSC curves of the melt-quenched OIMH glasses, showing the first and second heating processes. a). (But-bz)$MnBr_4$, b). (Pent-bz)$MnBr_4$, and c). (Hex-bz)$MnBr_4$.

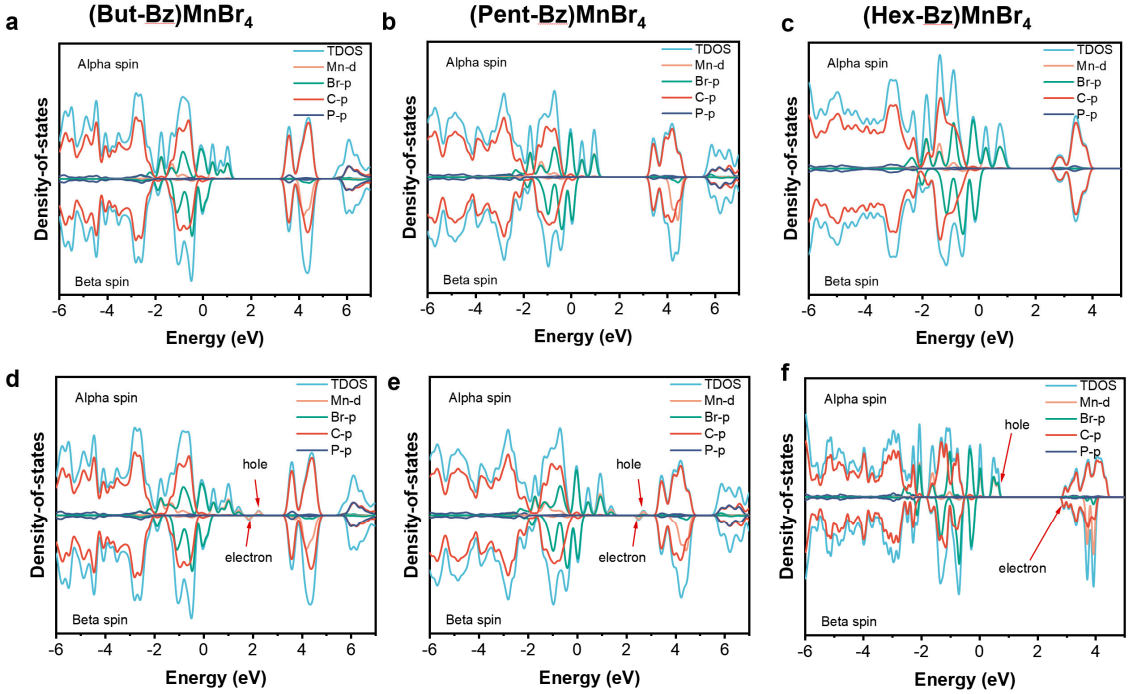

Figure S7. (a–c) Ground-state and (d-f) excited-state densities of states for (a, d) (But-bz)$MnBr_4$, (b, e) (Pent-bz)$MnBr_4$, and (c, f) (Hex-bz)$MnBr_4$.

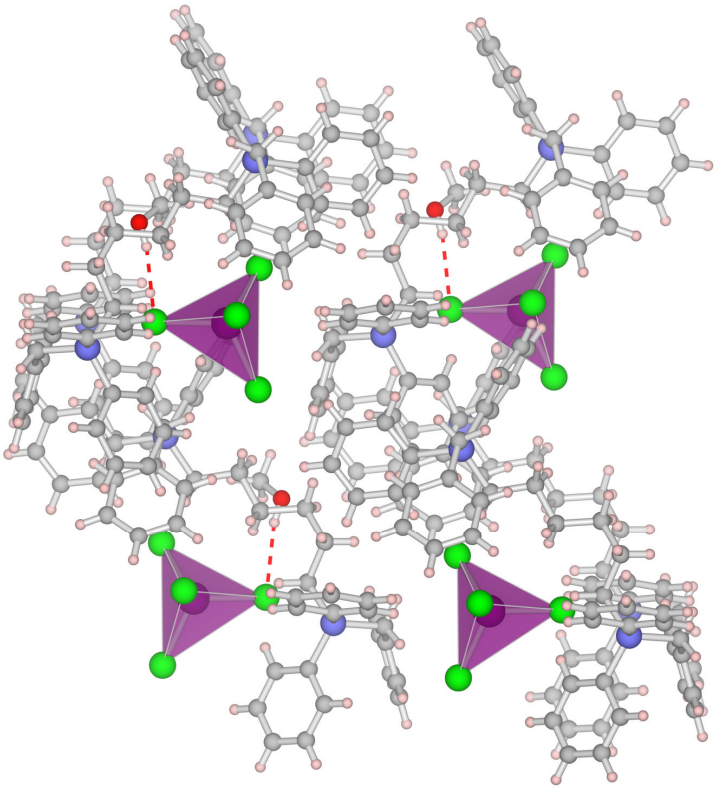

Figure S8. Crystal structure of (Hex-bz)$MnBr_4$·MeOH. The red dashed line shows the hydrogen bonding.

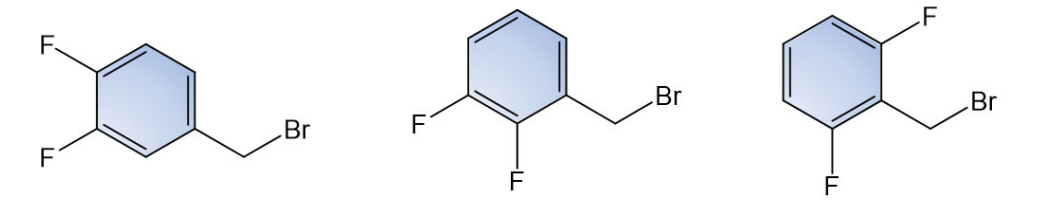

3,4-difluorobenzyl bromide 2,3-difluorobenzyl bromide 2,6-difluorobenzyl bromide

Figure S9. Three bromobenzyl derivatives used in the synthesis of BisPP-Br.

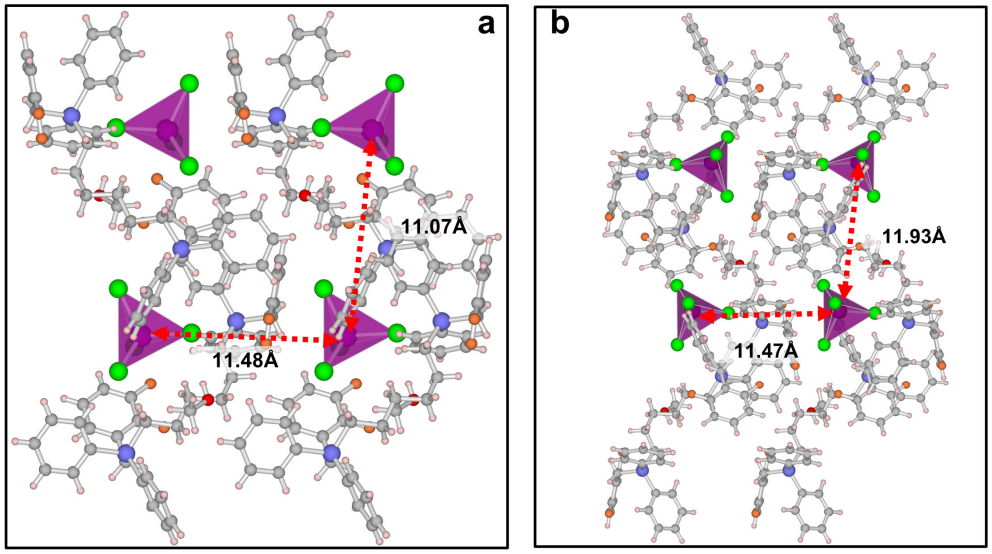

Figure S10. Crystal structures of a). (Hex-2,3-2F)$MnBr_4$·MeOH; b). (Hex-2,6-2F)$MnBr_4$·MeOH (grey: C, pink: H, blue: P, purple: Mn, green: Br, orange:F, Red:O).

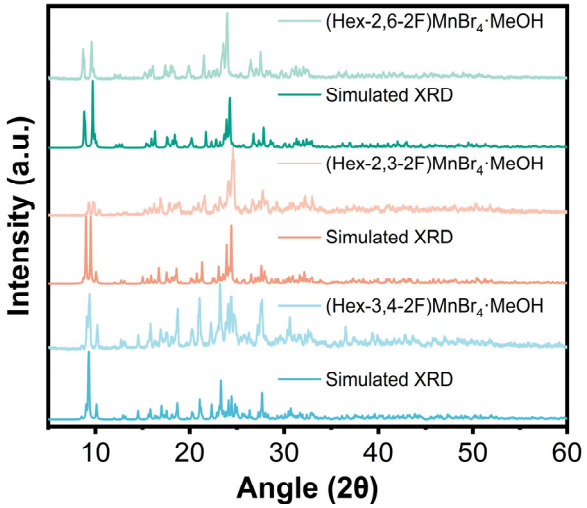

Figure S11. XRD patterns of the (Hex-3,4-2F)$MnBr_4$·MeOH, (Hex-2,3-2F)$MnBr_4$·MeOH, and (Hex-2,6-2F)$MnBr_4$·MeOH crystals.

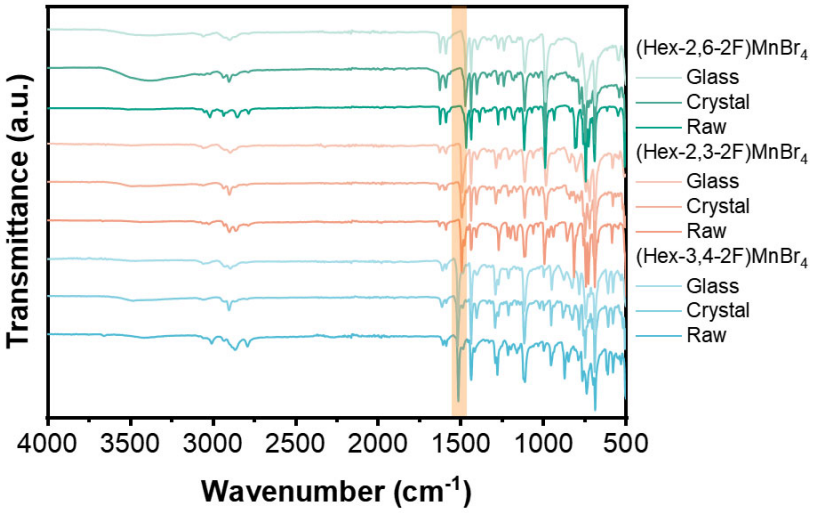

Figure S12. Attenuated total reflectance (ATR)-Fourier transform infrared spectra of the (BisPP)MnBr4 crystals and glasses. The curves labeled as *Raw* means the corresponding BisPP-Br. The curves labeled as *Crystal* mean the (BisPP)MnBr4 crystals containing solvent methol. The yellow area represents the C-F bond.

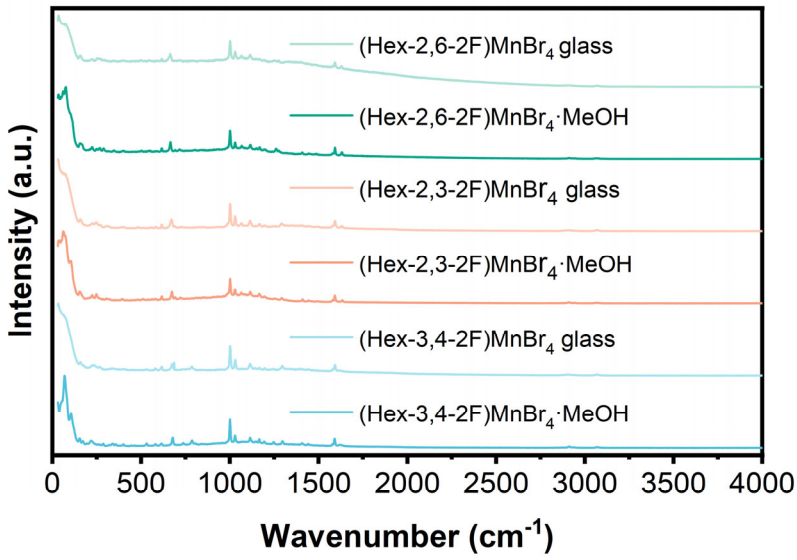

Figure S13. Raman spectra of (BisPP)MnBr4 crystals and glasses.

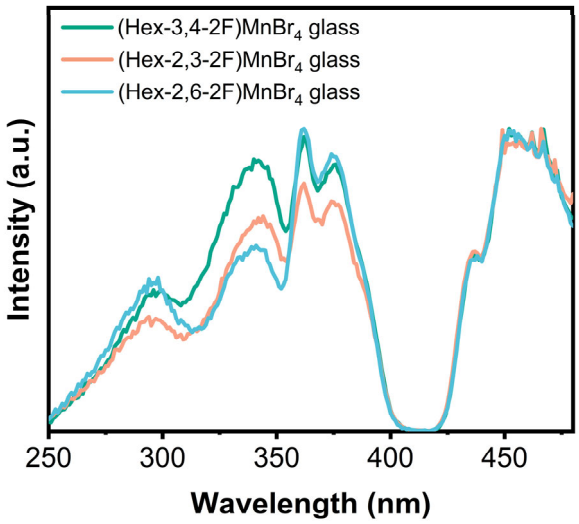

Figure S14. PLE plots of (Hex-3,4-2F)$MnBr_4$, (Hex-2,3-2F)$MnBr_4$ and (Hex-2,6-2F)$MnBr_4$ glasses.

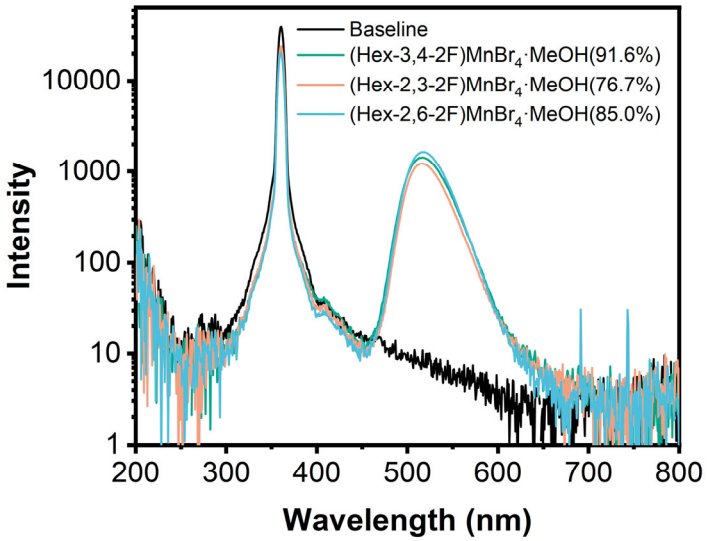

Figure S15. PLQY plots of the (Hex-3,4-2F)$MnBr_4$·MeOH, (Hex-2,3-2F)$MnBr_4$·MeOH and (Hex-2,6-2F)$MnBr_4$·MeOH crystal.

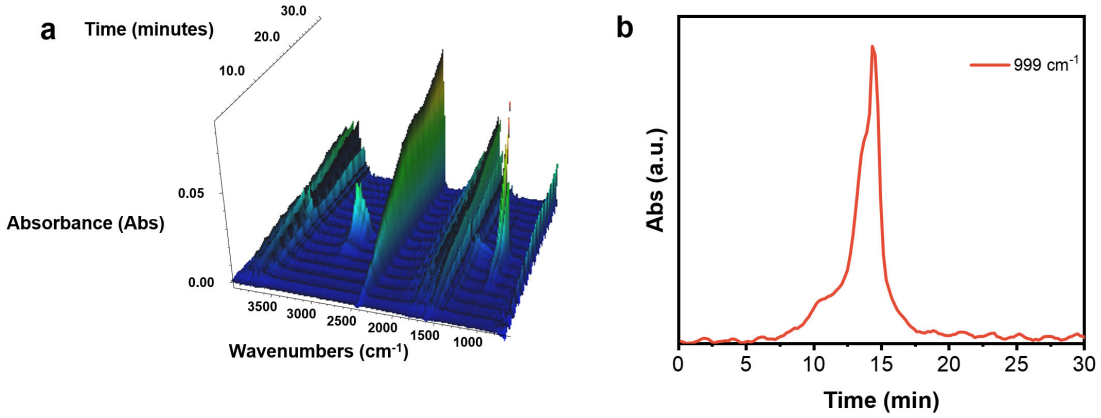

Figure S16. a). 3D map of the temperature-dependent IR spectra of (Hex-3,4-2F)$MnBr_4$·MeOH crystal. b). Monitoring one of the characteristic peaks of gas-phase methanol. TG-IR initiates at 30 ℃, ascending at a rate of 10 ℃/min. The timeframe of 11-16 minutes in Figure b approximately aligns with the temperature range of 140-190 ℃, coinciding with the melting process observed in DSC, wherein the primary gaseous product is methanol.

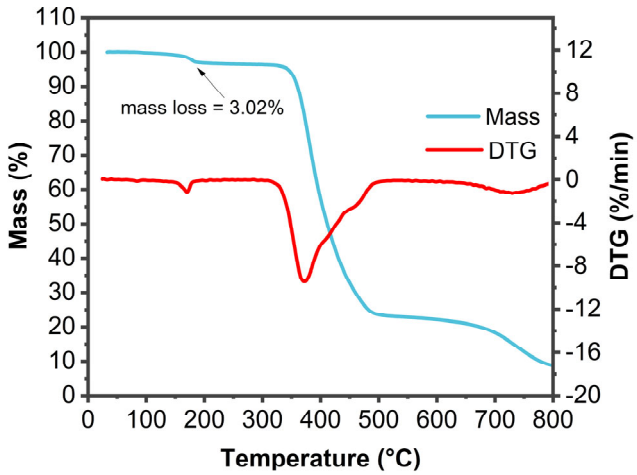

Figure S17. TG of the (Hex-3,4-2F)$MnBr_4$·MeOH crystal.

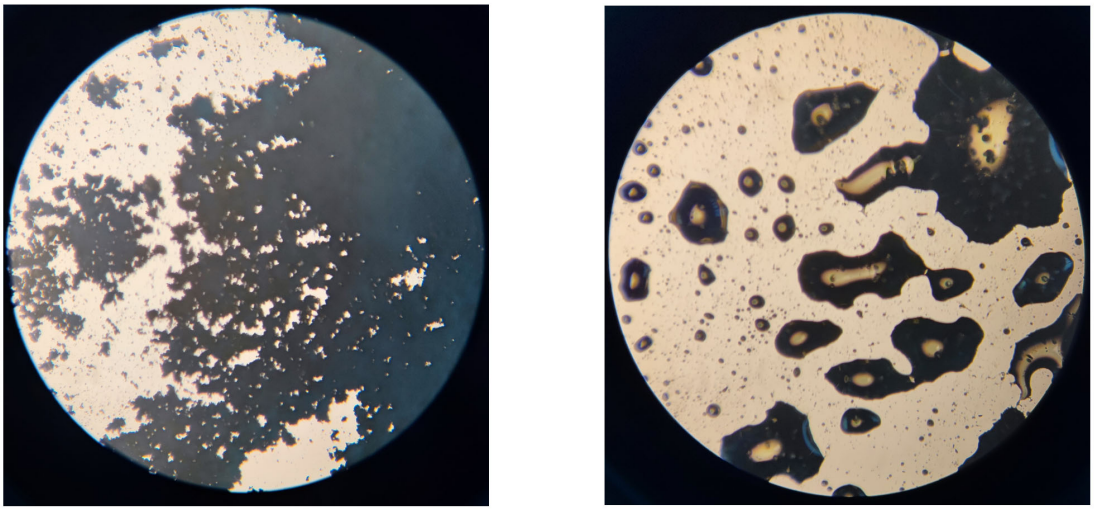

Figure S18. The (Hex-3,4-2F)$MnBr_4$·MeOH crystal melting observed under 5x magnification.

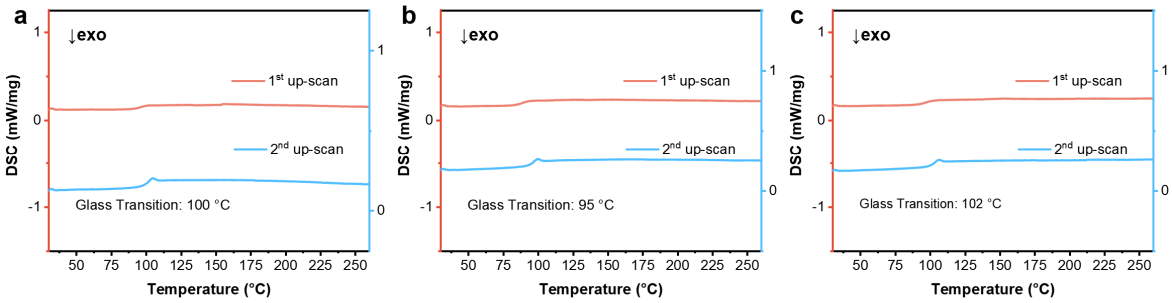

Figure S19. DSC curves of the a). (Hex-3,4-2F)$MnBr_4$; b). (Hex-2,3-2F)$MnBr_4$; c). (Hex-2,6-2F)$MnBr_4$ melt-quenched glass, showing the first and second heating processes.

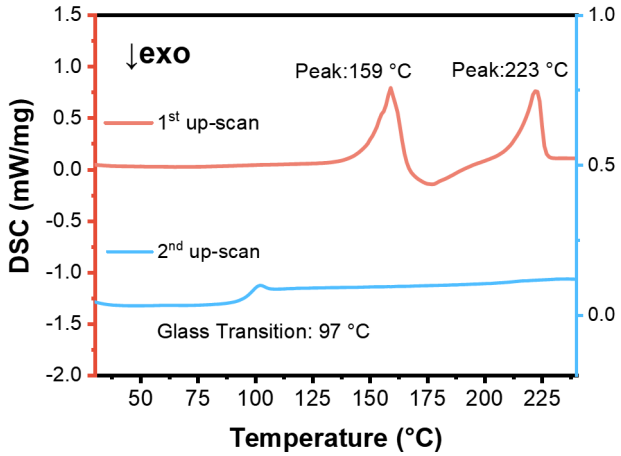

Figure S20. DSC curve of (Hex-bz)$MnBr_4$·MeOH. In the first up-scan, the first endothermic peak corresponds to the solvent removal, while the exothermic peak indicates recrystallization into a solvent-free phase ((Hex-bz)$MnBr_4$). The second endothermic peak corresponds to the melting of the (Hex-bz)$MnBr_4$.

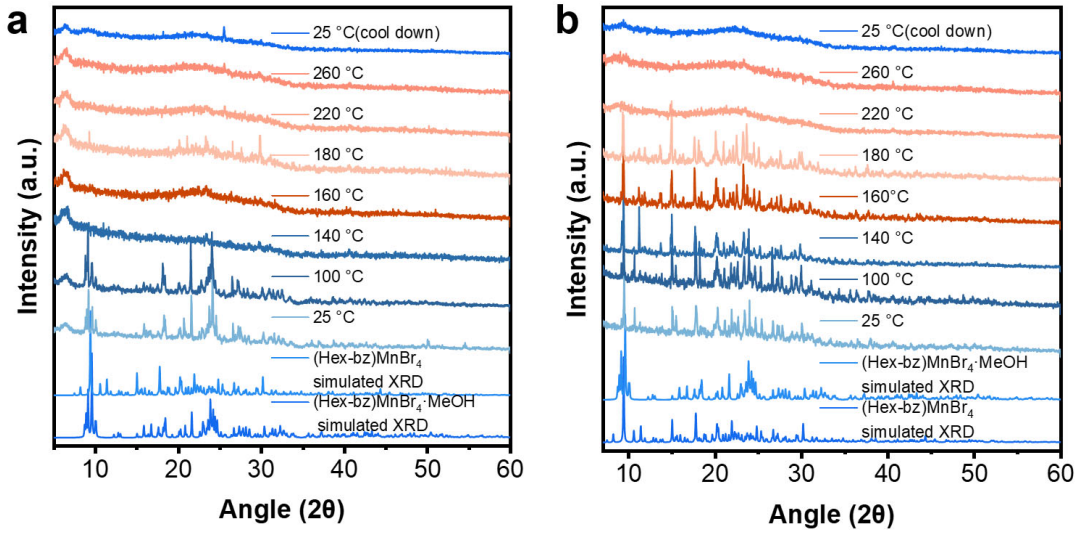

Figure S21. Temperature-dependent XRD patterns of a). (Hex-bz)$MnBr_4$·MeOH and b). (Hex-bz)$MnBr_4$.

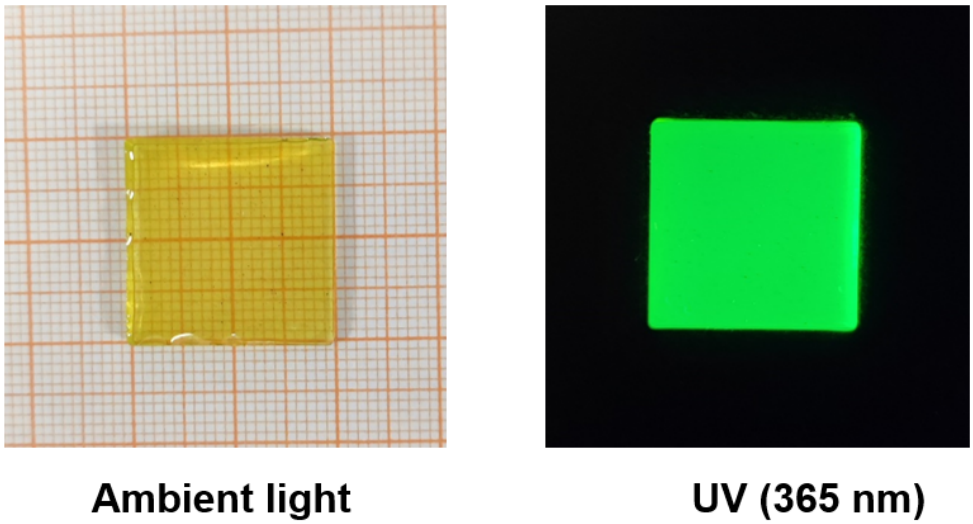

Figure S22. Pictures of (Hex-3,4-2F)$MnBr_4$ glass under ambient light and UV light.

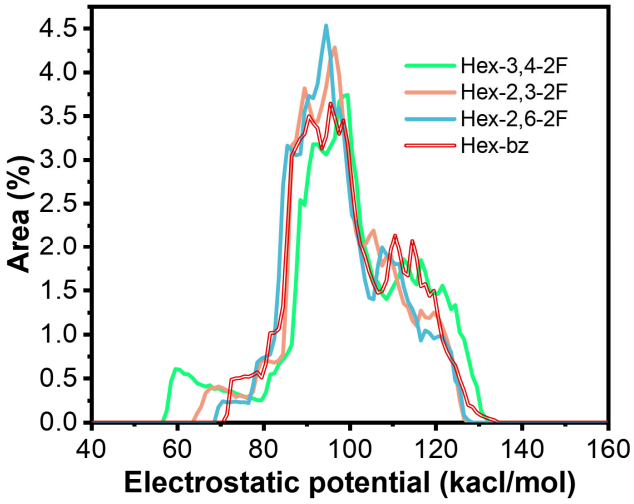

Figure S23. Surface electrostatic potential distribution of Hex-bz,Hex-3,4-2F, Hex-2,3-2F,Hex-2,6-2F cations.[7]

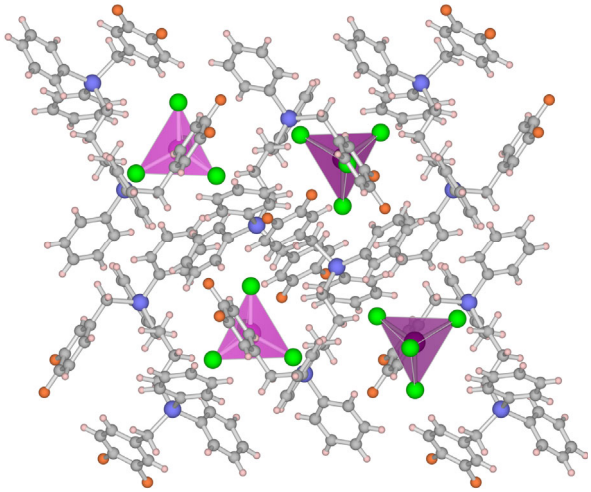

Figure S24. Crystal structure of (But-3,4-2F)$MnBr_4$.

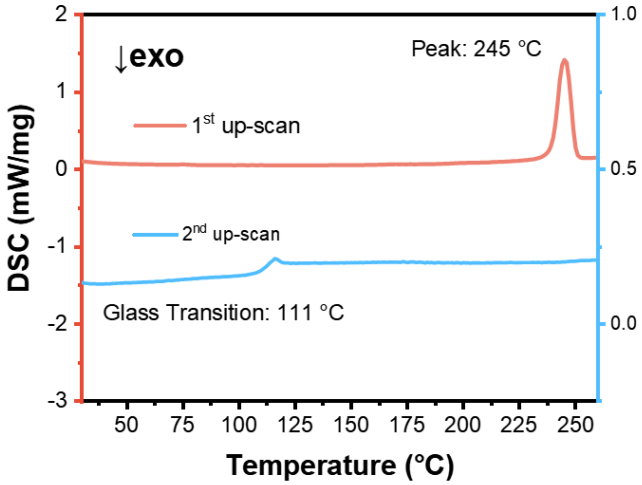

Figure S25. DSC curves of the (But-3,4-2F)$MnBr_4$ crystal.

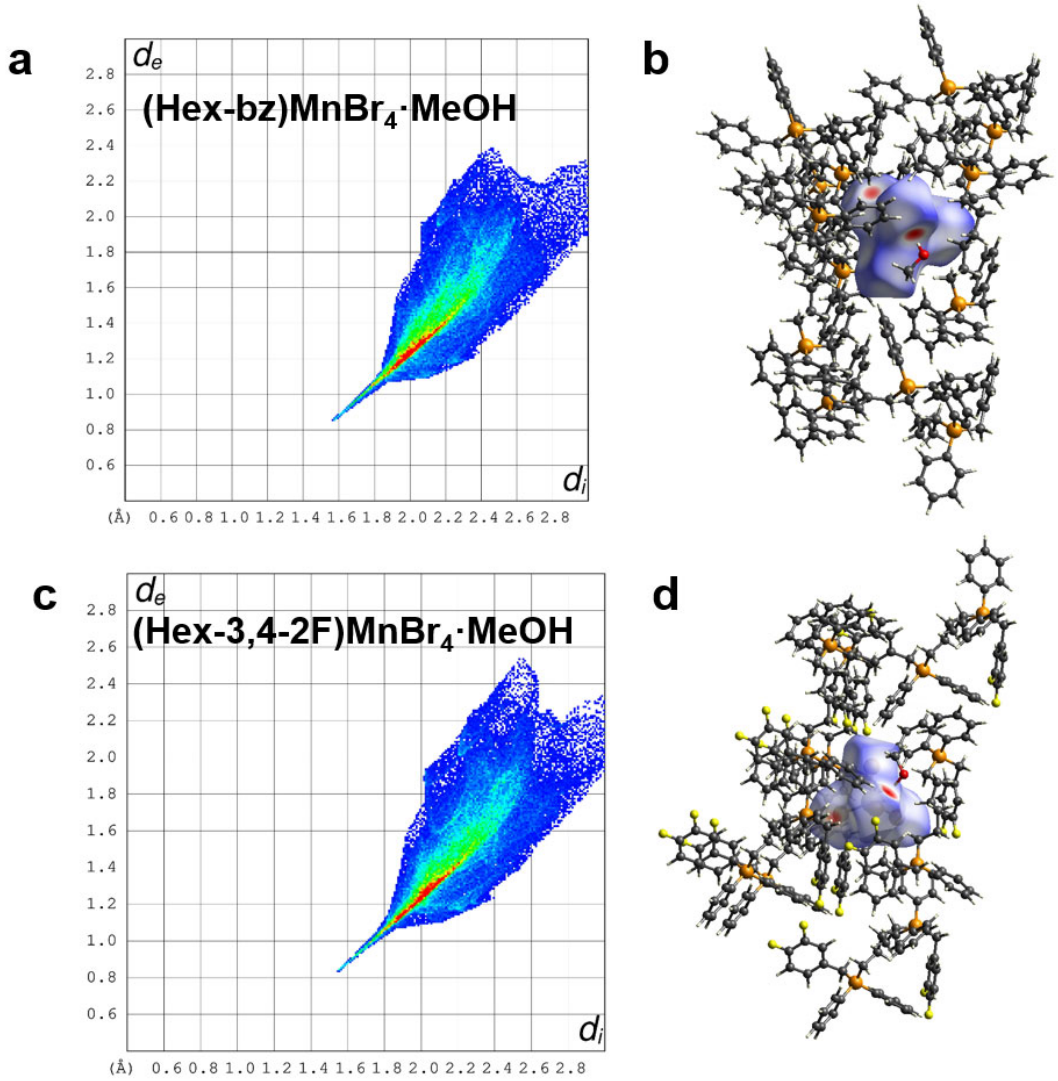

Figure S26. Hirshfeld analysis. a&c. Fingerprint plots of $[MnBr_4]^{2-}$ interaction. b&d d_{norm} surface. These results were obtained using CrystalExplorer software.[22]

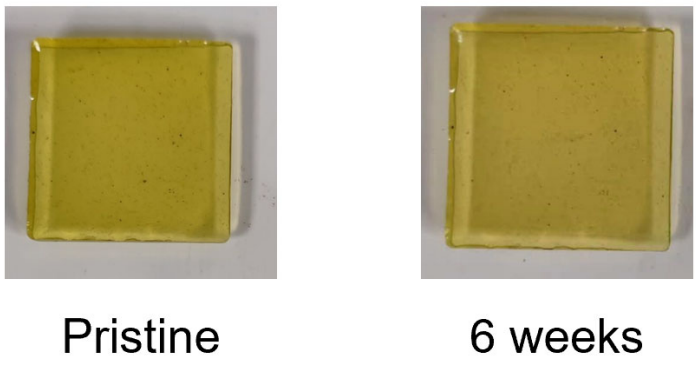

Figure S27. Thermostability test of (Hex-3,4-2F)$MnBr_4$ glass.

Supplementary References

1. K. Momma and F. Izumi, *J. Appl. Crystallogr.*, 2011, **44**, 1272-1276.
2. T. Jiang, W. Ma, H. Zhang, Y. Tian, G. Lin, W. Xiao, X. Yu, J. Qiu, X. Xu, Y. Yang and D. Ju, *Adv. Funct. Mater.*, 2021, **31**, 2009973.
3. M. J. Frisch, G. W. Trucks, H. B. Schlegel, G. E. Scuseria, M. A. Robb, J. R. Cheeseman, G. Scalmani, V. Barone, G. A. Petersson, H. Nakatsuji, X. Li, M. Caricato, A. V. Marenich, J. Bloino, B. G. Janesko, R. Gomperts, B. Mennucci, H. P. Hratchian, J. V. Ortiz, A. F. Izmaylov, J. L. Sonnenberg, Williams, F. Ding, F. Lipparini, F. Egidi, J. Goings, B. Peng, A. Petrone, T. Henderson, D. Ranasinghe, V. G. Zakrzewski, J. Gao, N. Rega, G. Zheng, W. Liang, M. Hada, M. Ehara, K. Toyota, R. Fukuda, J. Hasegawa, M. Ishida, T. Nakajima, Y. Honda, O. Kitao, H. Nakai, T. Vreven, K. Throssell, J. A. Montgomery Jr., J. E. Peralta, F. Ogliaro, M. J. Bearpark, J. J. Heyd, E. N. Brothers, K. N. Kudin, V. N. Staroverov, T. A. Keith, R. Kobayashi, J. Normand, K. Raghavachari, A. P. Rendell, J. C. Burant, S. S. Iyengar, J. Tomasi, M. Cossi, J. M. Millam, M. Klene, C. Adamo, R. Cammi, J. W. Ochterski, R. L. Martin, K. Morokuma, O. Farkas, J. B. Foresman and D. J. Fox, Gaussian 16 Rev. C.01.*Journal*, 2016.
4. J. Hutter, M. Iannuzzi, F. Schiffmann and J. VandeVondele, *Wiley Interdiscip. Rev.: Comput. Mol. Sci.*, 2014, **4**, 15-25.
5. T. Lu and F. Chen, *J. Comput. Chem.*, 2011, **33**, 580-592.
6. S. Manzetti and T. Lu, *J. Phys. Org. Chem.*, 2013, **26**, 473-483.
7. J. Zhang and T. Lu, *Phys. Chem. Chem. Phys.*, 2021, **23**, 20323-20328.
8. L. J. Xu, X. Lin, Q. He, M. Worku and B. Ma, *Nat. Commun.*, 2020, **11**, 4329.
9. T. Xu, W. Li, Z. Zhou, Y. Li, M. Nikl, M. Buryi, J. Zhu, G. Niu, J. Tang, G. Ren and Y. Wu, *Phys. Status Solidi RRL*, 2022, **16**, 2200175.
10. P. Fu, Y. Sun, Z. Xia and Z. Xiao, *J. Phys. Chem. Lett.*, 2021, **12**, 7394-7399.
11. B. Li, Y. Xu, X. Zhang, K. Han, J. Jin and Z. Xia, *Adv. Optical Mater.*, 2022, **10**, 2102793.
12. B. Li, J. Jin, M. Yin, X. Zhang, M. S. Molokeev, Z. Xia and Y. Xu, *Angew. Chem. Int. Ed.*, 2022, **61**, e202212741.
13. M. I. Ojovan, *JETP Lett.*, 2004, **79**, 632-634.
14. J. B. Luo, J. H. Wei, Z. Z. Zhang, Z. L. He and D. B. Kuang, *Angew. Chem. Int. Ed.*, 2023, **62**, e202216504.
15. Z. L. He, J. H. Wei, J. B. Luo, Z. Z. Zhang, J. H. Chen, X. X. Guo and D. B. Kuang, *Laser Photonics Rev.*, 2024, DOI: 10.1002/lpor.202301249.
16. Y. Xu, Z. Li, G. Peng, F. Qiu, Z. Li, Y. Lei, Y. Deng, H. Wang, Z. Liu and Z. Jin, *Adv. Optical Mater.*, 2023, **11**, 2300216.
17. B. Li, J. Jin, M. Yin, K. Han, Y. Zhang, X. Zhang, A. Zhang, Z. Xia and Y. Xu, *Chem. Sci.*, 2023, **14**, 12238-12245.
18. C. Dong, X. Song, B. E. Hasanov, Y. Yuan, L. Gutiérrez-Arzaluz, P. Yuan, S. Nematulloev, M. Bayindir, O. F. Mohammed and O. M. Bakr, *J. Am. Chem. Soc.*, 2024, **146**, 7373-7385.

19. B. Li, J. Jin, X. Liu, M. Yin, X. Zhang, Z. Xia and Y. Xu, *ACS Mater. Lett.*, 2024, **6**, 1542-1548.
20. T. Feng, Z. a. Zhou, Y. n. An, L. Chen, Y. Fu, S. Zhou, N. Wang, J. Zheng and C. Sun, *ACS Nano*, 2024, **18**, 16715-16725.
21. Z. Xu, N. Li, X. Yan, X. Wang, T. He, Z. Yang and S. Liu, *Adv. Optical Mater.*, 2023, **12,** 2301477.
22. P. R. Spackman, M. J. Turner, J. J. McKinnon, S. K. Wolff, D. J. Grimwood, D. Jayatilaka and M. A. Spackman, *J. Appl. Crystallogr.*, 2021, **54**, 1006-1011.